Published in final edited form as:
Biochemistry. 2013 February 26; 52(8): 1354–1363. doi:10.1021/bi301566v.

Thermodynamic Profiles and NMR Studies of Oligonucleotide Duplexes Containing Single Diastereomeric Spiroiminodihydantoin Lesions

Irine Khutsishvili[†], **Na Zhang**[‡,‖], **Luis A. Marky**[†], **Conor Crean**[§,#], **Dinshaw J. Patel**[‡], **Nicholas E. Geacintov**[§], and **Vladimir Shafirovich**[*,§]

[†]Department of Pharmaceutical Sciences, University of Nebraska Medical Center, Omaha, NE 68198-4628, United States

[‡]Cellular Biochemistry and Biophysics Program, Memorial Sloan Kettering Cancer Center, New York, New York 10021, United States

[§]Chemistry Department, New York University, 31 Washington Place, New York, New York 10003-5180, United States

Abstract

The spiroiminodihydantoins (Sp) are highly mutagenic oxidation products of guanine and 8-oxo-7,8-dihydroguanine in DNA. The Sp lesions have been recently detected in the liver and colon of mice infected with *H. hepaticus* that induces inflammation and development of liver and colon cancers in murine model systems [Mangerich, A., et al. (2012) *Proc. Natl. Acad. Sci. U.S.A. 109*, E1820–E1829]. The impact of Sp lesions on the thermodynamic characteristics and the effects of the diastereomeric Sp-*R* and Sp-*S* lesions on the conformational features of double-stranded 11-mer oligonucleotide duplexes have been studied by a combination of microcalorimetric, analysis of DNA melting curves, and two-dimensional NMR methods. The non-planar, propeller-like shapes of the Sp residues strongly diminish the local base stacking interactions that destabilize the DNA duplexes characterized by unfavorable enthalpy contributions. Relative to an unmodified duplex, the thermally induced unfolding of the duplexes with centrally positioned Sp-*R* and Sp-*S* lesions into single strands is accompanied by a smaller release of cationic counterions (Δn_{Na+} = 0.6 mol Na^+ per mol duplex) and water molecules (Δn_w = 17 mol H_2O per mol duplex). The unfolding parameters are similar for the Sp-*R* and Sp-*S* lesions although their orientations in the duplexes are different. The structural disturbances radiate one base pair beyond the flanking C:G pair, although Watson-Crick hydrogen bonding is maintained at all flanking base pairs. The observed relatively strong destabilization of B-form DNA by the physically small Sp lesions are expected to have a significant impact on the processing of these lesions in biological environments.

[*]Corresponding Author: V. Shafirovich, vs5@nyu.edu, Tel: (212) 998-8456.
[‖]High Magnetic Field Laboratory of the Chinese Academy of Sciences, Hefei, Anhui, 230031, China
[#]Laboratory and Scientific Section Division for Policy Analysis and Public Affairs United Nations Office on Drugs and Crime, P.O. Box 500, 1400 Vienna, Austria

The authors declare no competing financial interest

Supporting Information

Supplemental Figures 1 – 3, showing 2-D NMR NOE and COSY spectra of site specifically modified 11-mer duplexes containing the Sp-*S* lesion. This material is available free of charge via the Internet at http://pubs.acs.org.

Introduction

Chronic inflammation plays a critical role in the initiation and progression of many human cancers (1). The inflammatory response activates macrophages and neutrophils to produce free radicals, strong oxidizing agents and other chemokines that generate persistent oxidative stress in inflamed tissues (2). The reactive chemical mediators of inflammation are capable of damaging cellular DNA to form a wide spectrum of DNA base modifications (3). Many of these lesions are genotoxic; if not removed by the DNA repair machinery, these lesions can contribute to the mutagenic burden of the cells and ultimately the development of cancer (4). The fundamental mechanism of formation of DNA damage by the actions of certain oxidizing species overproduced at sites of inflammation, can be viewed as a series of consecutive one-electron oxidations of guanine (5), the most easily oxidizable nucleic acid base in DNA (6). The best known, stable lesion derived from the abstraction of even numbers of electrons, is the well-known mutagenic biomarker of oxidative stress, 8-oxo-7,8-dihydroguanosine (8-oxoG), the product of a two-electron oxidation of guanine (7). Although, the levels of 8-oxoG in cellular DNA are quite small, in the range of ~ 0.3–4 8-oxoG residues per 10^6 guanines (8), 8-oxoG is very prone to further oxidation (9) and can be selectively oxidized by weak one-electron oxidants such as Fe(III) complexes even in the presence of an excess of guanine bases (10). The stable products of a two-electron oxidation of 8-oxoG are the spiroiminodihydantoin (Sp) and guanidinohydantoin (Gh) lesions (11–13). These hydantoins are highly mutagenic leading to transversion mutations (G → T and G → C) (14). In vitro, the hydantoin lesions are efficiently repaired by base excision repair enzymes that involve the *E. coli* Fpg (15), Nei (16), mammalian NEIL1 and NEIL2 (17), and human NEIL1 (18, 19) DNA glycosylases. The accumulation of Sp lesions was detected in Nei-deficient *E. coli* after treatment of these cells by chromate (20). Recently, the Sp/Gh lesions were detected in both the liver and colon of mice at levels of ~100 times lower than those observed for 8-oxoG (21). However, the basal level of Sp and Gh can contribute to the malignant transformations in cells given that Sp is at least one order of magnitude more mutagenic than 8-oxoG (14). Indeed, cellular levels of Sp lesions were modestly correlated with the progression of the disease in a mouse model of inflammation-induced colon cancer (21).

In aqueous solutions, Gh readily interconverts to iminoallantoin (Ia) via enolization, and the Gh/Ia isomers exist in an equilibrium that depends on the pH of the solution (12). In turn, spiroiminodihydantoin exists as a pair of diastereomers, Sp-*R* and Sp-*S* (11, 22) (Figure 1A), which are stable, can be isolated by HPLC methods, and their absolute configurations can be identified by optical rotatory dispersion (ORD) and circular dichroism (CD) methods (23–25). As discussed in more detail elsewhere (23, 26), the stereoisomeric Sp lesions can exist either in the amino or imino tautomeric forms; however, the calculations suggest that the amino forms are favored by ~ 1 kcal/mol over the imino form and are thus depicted in Figure 1. Our molecular mechanics calculations showed that the flexibility of the glycosidic torsion angles in both Sp diastereomers are significantly more restricted than in the case of unmodified 2′-deoxyguanosine (26). Computational analysis of the structures and energies suggested that the Sp lesions could adversely impact base stacking and Watson-Crick hydrogen bonding interactions in the double-stranded DNA, and cause a widening of both the minor and major grooves (27). However, these predictions were not verified experimentally. Some characteristics of the Sp lesions are well known, however. For example, the Sp lesions are substrates of the human NEIL1 glycosylase (28), and cause a significant destabilization of double-stranded DNA (29–31). In this work we compare the thermodynamic characteristics of the Sp-*R* and Sp-*S* diastereomeric lesions positioned in the center of 11-mer oligonucleotide duplexes (Figure 1B) as a function of DNA concentration, ionic strength, and thermodynamic water activity. The impact of the two Sp diastereoisomers on the structural characteristics of double-stranded 11-mer

oligonucleotides were examined by standard solution NMR methods that are compared here to the thermodynamic properties of the same duplexes.

Materials and Methods

Preparation of Samples

The oligonucleotide adducts containing enantiomeric Sp nucleobases (Figure 1A) were prepared by oxidation of 5′-d(CCATCGCTACC) sequences by photochemically generated carbonate radical anions (32, 33). The samples containing 10 μM 5′-d(CCATCGCTACC) (Figure 1B), 10 mM $Na_2S_2O_8$ and 300 mM $NaHCO_3$ in air-equilibrated phosphate buffer solution (pH 7.5–8.0) were exposed to continuous light of a 100 W xenon arc lamp reflected from a dichroic mirror to select the 300–340 nm spectral range. The energy incident on the sample was ~100 mW/cm^2, and the irradiation time was 20–30 s. After irradiation, the sample was immediately desalted by reversed-phase HPLC, concentrated, and subjected to anion-exchange HPLC analysis. The oxidatively modified oligonucleotides were isolated by anion-exchange HPLC with an analytical (250×4 mm i.d.) DNAPac PA-100 column (Dionex, Sunnyvale, CA) and a 10–90% linear gradient of solvent B (10% acetonitrile and 90% 1.5 M ammonium acetate) in solvent A (10% acetonitrile and 90% water) for 30 min at a flow rate of 1 mL/min. The solutions were desalted with an analytical (250 mm×4.6 mm i.d.) Microsorb-MV C18 column (Varian, Walnut Creek, CA) and the following mobile phases: ammonium acetate (5 mM, 10 min), water (10 min), and an isocratic acetonitrile/H_2O mixture (50:50, 15 min).

Stereochemistry

The anion-exchange HPLC elution profiles of the purified 11-mer oligonucleotides (denoted by oligo-Sp-*R* or oligo-Sp-*S*) containing either one or the other diastereomeric Sp lesion are depicted in Figure 1C. To determine the absolute configurations of the diastereomeric lesions the oligonucleotide adducts were digested to the level of nucleobases by a soft acid hydrolysis of the dry oligonucleotide samples in HF/pyridine solution at 37 °C (22, 23). The isolation of Sp nucleobases was performed in two steps. The digestion mixture was first separated by reversed-phase HPLC with an analytical Microsorb-MV C18 column that does not retain the Sp nucleobases. The void volume from this reversed-phase HPLC run was collected, dried and resuspended in the HPLC mobile phase (see, below). Pure Sp nucleobases were obtained in a second HPLC experiment using a Hypercarb column (100 mm×3 mm i.d., Thermo Electron Corp.) using an isocratic mobile phase (98:2 water/acetonitrile solvent containing 0.5% formic acid). The Sp nucleobases excised from the oligonucleotide adducts were identified by optical rotatory dispersion and circular dichroism methods (23–25). The Sp nucleobase excised from the adduct eluted at 16.2 min (fraction #1) was characterized by a positive CD signal at 235 nm, and negative CD signals at 213 and 255 nm (Figure 1D), as well as a negative ORD signal in the > 300 nm region (data not shown), and thus had "*R*" absolute configuration (23–25). The Sp nucleobase obtained from HPLC fraction #2 eluted at 18.4 min, exhibited CD and ORD spectra that were mirror images of those obtained with the Sp nucleoside derived from fraction #1, with a negative CD signal at 235 nm, positive CD signals at 213 and 255 nm (Figure 1D), and a positive ORD signal in the > 300 nm region (data not shown). Thus, the oligonucleotide in fraction #2 contains the Sp lesion with "*S*" absolute configuration (23–25). We note that the assignment of the HPLC elution order is insufficient for correctly identifying the Sp stereoisomers, because the elution order of the Sp diastereomeric adducts reported here, with the Sp-*R* diastereomer eluting first using an anion exchange column (Figure 1C), can be reversed by using reversed-phase HPLC columns (32). In the case of dSp nucleosides, which have very similar CD/ORD spectra to those shown for the base forms Sp (23), the *R* dSp stereoisomer elutes first when a normal-phase amino NH_2-Hypersil column is utilized, as

reported by Ravanat and Cadet (22); however, this order of elution is reversed when a Hypercarb column is used (23, 34). It is therefore necessary to specify the CD and/or ORD of each fraction in order to determine the chiro-optical properties of the enzymatic digestion products of the Sp-containing oligonucleotides to the Sp nucleoside or base levels by determining their CD (or ORD) spectra (Figure 1D). The assignments of the *R* and *S* absolute configurations used in this work are based on comparisons of the experimentally measured and computed CD and ORD spectra of the Sp/dSp diastereoisomers as described in detail elsewhere (23–25). We note, however, that Karwowski et al. (35), on the basis of 2D NOESY NMR spectra of dSp stereoisomers dissolved in dimethylsulfoxide solution with low levels of residual water, arrived at the opposite assignments. For simplicity, we will refer to the modified double-stranded 5′-d(CCATC[Sp]CTACC)•5′-d(GGTAGCGATGG) molecules defined in Figure 1B, as the Sp-*R* or Sp-*S* 11-mer duplexes with defined stereochemical properties and HPLC elution orders identified in Figure 1.

In order to ensure 1:1 strand stoichiometry of the modified duplexes, we measured job plots to determine the molar extinction coefficients (ε_{260}) at 80 °C of the single-stranded oligonucleotides. The values obtained for the Sp-containing oligonucleotides were: Sp-*S* (ε_{260} = 86,000 M^{-1} cm^{-1}) and Sp-*R* (ε_{260} = 84,000 M^{-1} cm^{-1}), relative to the ε-value of the unmodified complementary strand (ε_{260} = 115,000 M^{-1} cm^{-1}).

Differential Scanning Calorimetry

The changes in heat capacity (C_P) as a function of temperature were determined with a VP-DSC differential scanning calorimeter (Microcal Inc., Northampton, MA). The oligonucleotide duplexes were dissolved in 20 mM sodium phosphate buffer (pH 7.0) and 0.1 M NaCl. All heat capacity profiles were determined against a reference buffer solution in the temperature range of 3 °C to 103 °C and a 0.75 °C/min scanning rate. The thermodynamic characteristics of the double strand → single strand transitions were determined as usual utilizing the equations for the changes in enthalpy, entropy, and free energy, using the respective thermodynamic equations (36):

$$\Delta H_{\mathrm{cal}} = \int \Delta C_P \, \mathrm{d}T \quad (1)$$

$$\Delta S_{\mathrm{cal}} = \int (\Delta C_P / T) \, \mathrm{d}T \quad (2)$$

$$\Delta G^{\circ}(T) = \Delta H_{\mathrm{cal}} - T\Delta S_{\mathrm{cal}} \quad (3)$$

With *H*, *S*, *G*, and C_P denoting the enthalpy, entropy, free energy, and heat capacity at constant pressure, respectively. The calorimetric van't Hoff enthalpies, $\Delta H_{\mathrm{vH}}^{\mathrm{cal}}$, were obtained from shape analysis of the heat capacity thermograms using the Origen software provided by the manufacturer.

UV Absorbance vs. Temperature Melting Curves

The DNA samples were contained in 10×10 mm square Quartz cuvettes. The UV absorbance at 260 nm (A_{260}) was measured as a function of temperature within the temperature range of 0° – 80 °C with the cuvette positioned within the thermoelectrically controlled sample holder of a Lambda-10 Perkin-Elmer spectrophotometer. The melting points, T_{M}, were determined from the midpoints of the A_{260} vs. *T* duplex → single strand melting curves. The van't Hoff enthalpy changes, $\Delta H_{\mathrm{vH}}^{\mathrm{UV}}$, were determined from the slopes of the linear plots of the experimentally measured values of $1/T_{\mathrm{M}}$ vs. $\ln(C_T/4)$, where

C_T is the total concentration of DNA strands. The values of the entropy change, ΔS_{vH}, were calculated from the intercept of these linear plots as described in detail elsewhere for non-self-complementary strands (36).

UV melting curves were also determined at different salt concentrations (carried out in the range of 30–225 mM NaCl at pH 7.0 to determine the differential thermodynamic release (or uptake) of counterions, Δn_{Na+}, and of water molecules, Δn_w, that accompany the dissociation of each DNA duplex to single strands. The thermodynamic relationship describing these terms are (37):

$$\Delta n_{Na+} = 0.483\ (\Delta H_{cal}/RT_M^2)(\partial T_M/\partial \log[Na^+]) \quad (4)$$

and

$$\Delta n_w = 0.483\ (\Delta H_{cal}/RT_M^2)(\partial T_M/(\partial \log[a_w])) \quad (5)$$

where a_w is the activity of water, and R is the molar gas constant. UV melting curves were determined at different concentrations of ethylene glycol (0.5 M – 4.0 M), and the activities a_w were calculated from osmolality measurements as described elsewhere (38, 39).

The first bracketed terms in equations 4 and 5 were experimentally determined from differential scanning calorimetry experiments, while the second bracketed terms in these equations were determined by measurements of T_M values at different NaCl or ethylene glycol concentrations, respectively.

NMR Methods

The 1D and 2D NMR experiments were carried out using a Varian INOVA 600 MHz spectrometer and the solution conditions are identified in Figures 6 and 7, and in the Supplementary Information section. The NMR data sets were processed using Varian software and analyzed using the FELIX program (Accelrys, Inc.).

Results

Thermodynamics

The differential scanning calorimetry curves for the X = Sp-*S*, X = Sp-*R*, and unmodified (X = C) duplexes are compared in Figure 2. The thermodynamic values ΔH_{cal} and ΔS_{cal} were evaluated from these curves according to equations 1 and 2, while $\Delta G°$(20 °C) was calculated from equation 3. These values are summarized in Table 1.

The double-strand to single-strand dissociation UV absorbance profiles at 260 nm of the different 1:1 duplexes as a function of temperature, are compared in Figures 3A – 3C, and the T_M values are summarized in Table 1. These profiles show that at the lowest temperatures, below ~ 10 °C, the molecules are in the duplex state, while at higher temperatures, all curves are sigmoidal in shape which is characteristic of the unfolding of DNA duplexes. However, both Sp lesions cause a very strong thermal destabilization of the Sp-*R* and Sp-*S* duplexes, consistent with previous observations with different sequence contexts (29) and one of the two diastereomeric lesions (31). Analysis of the melting curves at different total concentrations of DNA strands, C_T, shows that the T_M values increase with increasing DNA concentration, as expected for the unimolecular dissociation of duplexes into two single strands. The dependence of the T_M values on C_T is given by the van't Hoff equation (36):

$$1/T_M = (R/\Delta H_{vH}^{UV}) \ln C_T + (\Delta S - R\ln 2)/\Delta H_{vH}^{UV} \quad (6)$$

where ΔH_{vH}^{UV} is the van't Hoff transition enthalpy. The values of ΔH_{vH}^{UV} and ΔH_{cal} are compared in Table 1 and are similar in value; this observation suggests that the unfolding of both the unmodified and Sp-containing duplexes can be approximated by a two-state model (36).

The melting curves of the unmodified and Sp-*R* and Sp-*S* duplexes measured at different salt concentrations in the range of 32 – 232 mM are depicted in Figures 4A, 4B and 4C, respectively. All melting curves are shifted to higher temperatures as the NaCl concentration is increased. The T_M values increase linearly as a function of ln[Na^+] as shown in Figure 4D. The stabilities, as reflected by the higher T_M values of all three types of duplexes, increase with increasing NaCl concentrations, consistent with the observation that salt favors the duplex state that is characterized by a higher charge density parameter. The Δn_{Na+} values can be calculated from equation 4 (Table 2), since the first term on the right can be directly evaluated from the DSC data, and the second term is equal to the slope of the linear plot shown in Figure 4D.

The single strand - double strand DNA equilibrium is also dependent on the activity of water, Δa_w (Eq 5), which can be experimentally varied by changing the concentration of ethylene glycol, as discussed earlier (e.g., (40, 41). As shown in Figures 5A–5C, increasing the ethylene glycol concentration from 0.5 M to 4 M, gradually shifts the melting curves from higher to lower temperatures, i.e., water favors the duplex state with a higher hydration. The dependence of the T_M values of each of the three types of duplexes are plotted as a function of ln a_w in Figure 5D. The change in moles of water released, Δn_w, can be calculated using equation 5 by evaluating the first term on the right side from the DSC ΔH_{cal} value and the slopes of the linear T_M vs. ln a_w plots (Table 2).

NMR

Exchangeable Proton Spectra: The Sp-R 11-mer duplex—The exchangeable proton 1D NMR spectrum of the 11mer duplex containing the *R* Sp lesion in H_2O buffer solution, pH 6.8 at 0 °C, is shown in Figure 6A. The observable imino proton resonances appear in the 12.0–14.0 ppm range which is expected for normal Watson-Crick base pairing in B-form DNA in the same sequence context (42). These and other resonances were assigned (Figure 6A) using standard procedures (43, 44).

An expanded regions of the NOESY contour plot (200 ms mixing time) for the same Sp-*R* duplex in aqueous buffer solution at 0 °C is shown Figure 6C. The observable NOEs (a–e) between some of the adjacent imino protons are identified in this figure. No imino – imino connectivities are observable between Sp and the adjacent G18 and G16 imino protons. These observations suggest that, in the absence of hydrogen bonding between base pairs, the imino proton NOEs become invisible because of line broadening effects due to rapid exchange with water protons. However, NOEs between G18-T4 and G16-T8 imino protons on the 5′- and 3′-sides of the Sp lesion, respectively, are observable. These and the other observed imino-imino connectivities suggest that Watson-Crick base pairing is intact on either side of the lesion in the 11-mer duplex. This conclusion is further supported by the observation of NOEs between exchangeable C(NH_2) amino and G(NH1) imino protons, and between T(NH3) imino and non-exchangeable A(H2) base protons on opposite strands of the 11-mer duplex (Figure 6B). Cross-peaks characteristic of the Watson-Crick base pairing are observed between all T(NH3)-A(H2) proton (f – i) and between C(NH_2) and G(NH1) protons (j,j′; l,l′; n,n′; p,p′; r,r′), except the terminal C11:G12 base pair. Further NOEs between the exchangeable G(NH1) and non-exchangeable C(H5) base protons are observed

at all base pairs except C11:G12. These observations indicate that B-form Watson-Crick base pairing is intact at all base pairs except at the lesion site and at the terminal C11:G12 base pair. The latter is weakened by terminal fraying phenomena.

Non-exchangeable Proton spectra: The Sp-R 11-mer duplex—An expanded region of the NOESY contour plot (200 ms mixing time) of the Sp-*R* 11-mer duplex in D_2O buffer solution at pH 6.8 and 10 °C is shown in Figure 7A. The NOE connectivities between the base protons (purine H8 or pyrimidine H6, 7.0 – 8.5 ppm) and their own H1′- and 5′-flanking deoxyribose H1′ protons (5.0 – 6.4 ppm) are traced as blue lines for the modified strand from C1 to C11, and as red lines for the unmodified strand from G12 to G22. The NOEs on the (Sp-*R*)-containing strand are well pronounced within the -C2-A3-T4-, and the -T8-A9-C10- sequences, thus indicating that the duplex has a right-handed, most likely B-form conformation in these flanking duplex DNA segments. The B-form assignment is favored over the A-form because random sequence DNA in aqueous buffer solutions at low salt concentrations (0.1 M NaCl) are known to assume the B-form, while the A-form exists in aqueous - organic solvent mixtures or at very high salt concentrations, i.e., under conditions of lowered water activities. Furthermore, previous studies of the aqueous solution NMR structures of the same oligonucleotide sequence (Figure 1), but with a different lesion at the position of the Sp, exhibit a 2′-endo sugar pucker conformation which is characteristic of B-DNA (45). The Sp residue does not have any base protons and thus the connectivities within the central -C5-[Sp]-C7- region are not observable. The connectivities between the Sp-flanking base pairs T4 and C5, as well as C7 and T8 are quite weak, which is consistent with the weak imino-amino proton connectivities observed for the C5:G18 and C7:G16 bases pairs; this is evident from the weak NOEs, p,p′ and r,r′, respectively, relative to the much stronger NOEs between C2:G21 (l,l′) and C10:G13 (n,n′) shown in Figure 6B.

On the unmodified strand (red trace in Figure 7A), connectivities can be traced within the G13-T14-A15-G16- and the –G18-A19-T20-G21- segments, while NOEs in the G16-C17-G18- segment are not discernible. Overall, it is clear that the central region of the duplex that includes the three base pairs (….-C5-[Sp-*R*]-C7-….)•(…G18-C17-G16-…), is significantly destabilized relative to the other flanking base pairs on either side of this central three base-pair sequence. Furthermore, the C17(H6 – H1′) NOE's are weaker than those of nearby bases, suggesting that C17 is not in its normal B-form position and is likely to be more mobile than its neighboring bases that maintain their Watson-Crick base pair properties, although the Watson-Crick hydrogen bonding appears to be somewhat weakened at the C5:G18 and C7:G16 flanking base pairs (Figure 6B, NOEs p,p′ and r,r′) due to line broadening.

The Sp-S 11-mer duplex—The NMR characteristics of the Sp-*S* 11-mer duplex in D_2O buffer solution were also studied and a portion of the 2D-NOESY contour plot is shown in Figure 7B. The connectivities can be traced via identifiable NOEs from C1 – C5 and from C7 – C11 (blue lines), and from G12 – G22 (red lines), which is quite similar to those of the Sp-*R* 11-mer duplex. In the Sp-*S* duplex, the C17(H6-H1′) NOE seems to be stronger than in the case of the Sp-*R* duplex, but there is no discernible NOE between C17 and G18 on the same strand in both cases. The C17-G16 NOE is in a region of the 2D plot where it overlaps or is close to the strong C17*(H5-H6) NOE in both the Sp-*S* and Sp-*R* duplexes. The weakened T4-C5, C7-T8 and G16-C17 and C17-G18 NOEs in the Sp-*S* duplex in the central (….-C5-[Sp-*R*]-C7-….)•(…G18-C17-G16-…) region are similar to the weak connectivities in the Sp-*R* 11-mer duplex. Expanded NOESY (200 ms mixing time) 2D contour plots, and the 1D NMR spectrum of the Sp-*S* 11-mer duplex in 100 mM NaCl, 10 mM sodium phosphate H_2O buffer solution are shown in Supporting Information (Figures S1 and S2). These spectra are similar to those exhibited by the Sp-*R* 11-mer duplex shown in Figure 6, except that the Watson-Crick imino-amino NOEs, and thus hydrogen-bonding, in the

G16:C7 (G16(NH1)-C7(NH_2)) and G18:C5 (G18(NH1)-C5(NH_2)) base pairs appears to be somewhat stronger in the 11-mer Sp-*S* than in the case of the Sp-*R* duplex.

Discussion

The melting points T_M determined from UV melting curves demonstrates that both the Sp-*R* and Sp-*S* lesions positioned in the middle of the 11-mer sequences cause significant thermal destabilization of the duplexes. This is consistent with the deviations from normal B-DNA conformation in the central three-base pair segment of the duplex containing the Sp lesions assessed from the analysis of the NMR characteristics of these sequences. Since the Sp residues do not have any non-exchangeable protons, while the imino protons exchange with water too rapidly to be observable, the differences in conformations of the Sp-*R* and Sp-*S* lesions could not be defined. However, it is evident that the Sp lesions cause structural perturbations within the central C5-Sp-C7 segment and the partial destabilization of the flanking G16:C7 and G18:C5 base pairs; the latter is evident from the somewhat broadened imino proton resonances of G16 and G18 (Figure 6A and Figure S1), and the loss or weakened NOEs in the sequential 'walk' connectivities from G16 to C17 and from C17 to G18. Furthermore, the G16:C5 and G18:C7 imono – amino proton connectivities are significantly weakened in the Sp-*R* duplex, and to a somewhat lesser extent in the Sp-*S* duplex. The normal fraying of the terminal base pairs at both ends of the duplexes, coupled with the short four-base pair segments of Watson-Crick base pairs on either side of the lesion, account for the dramatic decrease in the T_M values from ~ 54 °C in the unmodified duplexes to ~ 29 °C in the Sp duplexes.

The hyperchromicity, or the relative magnitude of the increase in absorbance resulting from the double-strand – single strand melting transition reflects the base-base van der Waals stacking interactions in double-stranded DNA. The percent hyperchromicity is defined as $\%H = [A_{260}(\text{ss}) - A_{260}(\text{ds})]/[A_{260}(\text{ds})]\times 100$, where A_{260} is the absorbance at 260 nm and ds and ss define the double- and single-stranded states, respectively. The $\%H$ value is ~18% for unmodified DNA and decreases to ~ 14 – 16% in the case of the Sp-*R* and –*S* duplexes, suggesting a finite loss of stacking interactions. This loss in hyperchromicity is consistent with the lower endothermic enthalpy change accompanying the dissociation of the Sp 11-mer duplexes into single strands. The lower stacking interactions can be explained in terms of the propeller-like orientations of the two spiroiminodihydantoin A and B-ring systems (Figure 1A) that decrease the van der Waals interactions with neighboring base pairs (26, 27). The structural and thermodynamic features of Sp-*R* and Sp-*S* lesions embedded in the same 11-mer duplex studied in this work (Figure 1B) have been studied earlier by computational methods (27). Molecular dynamics (MD) simulation studies suggested that intercalative conformations of both Sp-*R* and Sp-*S* lesions are favored in the major groove of B-DNA. This investigation showed that full intercalation of the propeller-like Sp A and B-rings (Figure 1A) is not favored because of severe distortions of the DNA duplex. Instead, the positioning of both the Sp-*R* and Sp-*S* stereoisomers is favored in the major groove, although conformations in the sterically more favored minor groove are also possible (27). Whatever the conformations, the MD simulations suggest that both Sp diastereomers cause severe perturbations of the local DNA conformation by opening the major and minor grooves, by perturbing Watson-Crick hydrogen bonding quality in adjacent base pairs, and by diminishing base stacking. Furthermore, these perturbations affect the normal structural parameters of adjacent base pairs as noted experimentally (Figures 6 and 7).

The thermodynamic parameters of dissociation of duplexes summarized in Table 1, indicates that the values of ΔH_{cal} and ΔH_{vH} are rather similar in value. This indicates that the unfolding of the unmodified and Sp-modified 11-mer duplexes is close to a two-state model (36). It is noteworthy that the free energies of melting are rather small, especially in

the case of the Sp-containing duplexes (Table 1), thus demonstrating the lower thermodynamic stabilities of the modified relative to the unmodified duplexes. These ΔG terms result from the compensation of unfavorable enthalpy and favorable entropy terms. The unfavorable ΔH terms correspond to the energy needed for disrupting base pair stacking interactions and rupture of hydrogen bonds, while the favorable entropy terms reflects contributions of the dissociation of one DNA molecule into two single strands, as well as the release of counterions and water molecules. Comparing the ΔH_{cal} and ΔH_{vH} columns with the $T\Delta S_{cal}$ column, in Table 1, it is evident that the Sp lesions cause a greater change in the ΔH_{cal} or ΔH_{vH} values than the $T\Delta S_{cal}$ values. Thus, enthalpic effects contribute more to the destabilization of duplexes caused by the Sp lesions than entropic effects that are associated with the release of counterions and water. The dominant contribution of the enthalpic term to the destabilization of Sp-duplexes is in agreement with the work of Chinyengeter and Jamieson (31) who investigated the themodynamic properties of a single Sp lesion embedded in a 15-mer duplex. They observed a 20 °C thermal destabilization of their 15-mer duplex. Our conclusions, based on the impact of both Sp lesions on the free energy and T_M values of the modified duplexes, is consistent with these results. However, in our experiments, the $\Delta T_M = T_M$ (unmodified duplex) − T_M (Sp-modified) value was ~30 °C (Table 1) instead of the reported value of 20 °C (31). The lower stabilities in our case can be attributed to the smaller-size 11-mer duplexes used in our study.

Previous modeling studies indicate that there is an orientational difference between the Sp-*R* and Sp-*S* residues (26). The O6 atom in the Sp B-ring (Figure 1A) tends to be oriented towards the 3′-end of the modified strand in the Sp-*R* case, while the same oxygen atom is directed towards the 5′-end. Thermodynamic analyses of these stereoisomeric structures in the same 11-mer duplexes indicate that the Sp-*R* stereoisomer is associated with a somewhat lower free energy than the Sp-*S* duplex (27). However, the experimental unfolding studies show that the free energy differences in the Sp-*R* and Sp-*S* duplexes cannot be distinguished within experimental error (Table 1).

Variations in salt concentration and activity of water exert pronounced effects on the thermodynamics of dissociation of the 11-mer double strands into single strands (Figures 4 and 5). The differences in moles of sodium ions bound to the double-stranded DNA and single stranded DNA is defined by $\Delta n_{Na+} = n_{Na+}$(ds) − n_{Na+}(ss) (Table 2). The differences in the key thermodynamic parameters, reflecting the differences between modified and unmodified duplexes, are summarized in Table 3. The positive Δn_{Na+} values reflect the greater charge density associated with the double-stranded molecules than with the single-stranded molecules. This effect is associated with the shielding of the repulsive interactions between adjacent negatively charged DNA phosphate groups by sodium ions that enhance the stability of B-DNA in aqueous solutions. Thus upon dissociation of the duplexes, a fraction of these positively charged counterions are released and Δn_{Na+} is therefore positive in sign (Table 2). In the case of the unmodified DNA, Δn_{Na+} = 2.65 Na+ ions per mole of duplex, or 2.65/20 = 0.13 sodium ions per phosphate group, which is characteristic of the melting of short oligonucleotide duplexes (46). The release of counterions is lower in both the Sp-*R* and Sp-*S* duplexes ($\Delta n_{Na+} \approx 2$, Table 2) than in the unmodified duplex (Δn_{Na+} = 2.65, Table 2). This indicates, assuming that the association of Na^+ ions with unmodified and Sp-modified single-stranded DNA in solution is similar, that the charge density is lower in the spiroiminodihydantoin-containing 11-mer duplexes than in the unmodified duplex. The differential counterion release upon melting of the duplexes, $\Delta n_{Na+} = \Delta n_{Na+}$ (Sp) − Δn_{Na+} (unmodified) is equal to 0.6 – 0.7 Na^+ ions per mole of duplex (Table 3). The loss of charge density is most likely localized within the central (….-C5-[Sp-*R*]-C7-….)•(…-G18-C17-G16-…) segment since the NMR data show that the structural distortions caused by the Sp lesions are largely confined to this central sequence. The lower charge density in the Sp 11-mer duplexes is consistent with a loss of base stacking interactions that result in greater

distances between adjacent phosphate groups. Analogous effects have been observed with minimal duplex distorting base analogs (38) and lesions such as 8-oxoguanine (47), and the highly distorting cis-Pt lesions (48), while $\Delta\Delta n_{Na+} \approx 0$ in duplexes with bulky benzo[*a*]pyrene diol epoxide-N^2-guanine adducts positioned in the minor groove of B-DNA with all Watson-Crick base pairs remaining intact (49).

The melting of double-stranded DNA is accompanied by the release of water molecules as well as positively charged counterions. The release of water can be determined by measuring the dependence of the unfolding constant of each DNA duplex on the activity of water, a_w (equation 5). It was shown earlier that ethylene glycol destabilizes DNA duplexes and diminishes T_M by lowering a_w only (50). The Δn_w values estimated from Figure 5D and equation 5 show that ~ 48 water molecules per mole of unmodified duplex are released during the melting process, while only ~ 30 molecules are released as a result of the dissociation of either of the two Sp 11-mer duplexes. The smaller number of water molecules released upon melting by the Sp 11-mer duplexes is consistent with (1) a smaller number of ordered structural, hydrogen-bonded water molecules in the grooves of DNA due to the disruptive effect of the Sp lesions, the widening of the grooves in its vicinity and concomitant disruption of hydrogen-bonded structures, and (2) a greater exposure of hydrophobic surfaces due to the non-planar propeller-like structure of the Sp base. This reduction in stacking interactions is accompanied by hydrophobic interactions of water molecules that have a higher enthalpy and entropy than structural, more ordered and better hydrogen-bonded structural water in the grooves of B-DNA (47). The latter effects contribute to the smaller enthalpy and entropy changes upon dissociation of the Sp duplexes to single strands.

Conclusions

Both Sp lesions cause similar extents of destabilization of double-stranded DNA that are associated with the non-planar, propeller-like orientations of the two rings that strongly diminish the local base stacking interactions. The smaller release of counterions and water point to an enhanced exposure of hydrophobic residues induced by the non-planar Sp lesions that also distort the local DNA backbone, thus requiring less screening of adjacent phosphate groups by sodium ions. The structural perturbations caused by the Sp lesions weaken the adjacent flanking Watson-Crick base pairs, but rupture the normal NOE connectivities between the central G18-C17-G16 nucleotides on the complementary strand with C17 being the partner base of Sp. The connectivities with nucleotides adjacent to G18 and G16, are also weakened so that the structural distortions radiate up to two base pairs beyond the Sp:C17 base pair. These structural features cause the same dramatic decrease in the melting points T_M of the Sp-*R* and Sp-*S* 11-mer duplexes. The thermodynamic and structural NMR characteristics established by NMR methods are remarkably similar for both Sp-*R* and Sp-*S* lesions. These properties predict that the biological response of these diastereomeric lesions by mechanisms that recognize structural DNA distortions caused by the lesions rather than the lesions themselves, e.g., nucleotide excision repair systems, is unlikely to be different for the Sp-*R* and Sp-*S* stereoisomers. On the other hand, recognition and incision by base excision repair has been shown to be different for the Sp-*R* and Sp-*S* lesions (51), most likely because the accommodation of the stereoisomeric Sp lesions into the active site of BER enzymes depends on their absolute configurations (28).

Supplementary Material

Refer to Web version on PubMed Central for supplementary material.

Acknowledgments

Funding

This work was supported by the National Institute of Environmental Health and Sciences Grant R01 ES 011589 (V.S.) at New York University, and by National Science Foundation Grants MCB-0616005 and MCB-1122029 (L.A.M.) at the University of Nebraska. Components of this work were conducted in the Shared Instrumentation Facility at NYU that was constructed with support from a Research Facilities Improvement Grant (C06 RR-16572) from the National Center for Research Resources, National Institutes of Health. The acquisition of the MALDI-TOF mass spectrometer was supported by the National Science Foundation (CHE-0958457).

Abbreviations

Sp	spiroiminodihydantoin
Gh	guanidinohydantoin
8-oxoG	8-oxo-7,8-dihydroguanine
Ia	iminoallantoin
DSC	differential scanning calorimetry
ORD	optical rotatory dispersion
CD	circular dichroism

References

1. Grivennikov SI, Greten FR, Karin M. Immunity, inflammation, and cancer. Cell. 2010; 140:883–899. [PubMed: 20303878]
2. Reuter S, Gupta SC, Chaturvedi MM, Aggarwal BB. Oxidative stress, inflammation, and cancer: How are they linked? Free Radic Biol Med. 2010; 49:1603–1616. [PubMed: 20840865]
3. Lonkar P, Dedon PC. Reactive species and DNA damage in chronic inflammation: Reconciling chemical mechanisms and biological fates. Int J Cancer. 2011; 128:1999–2009. [PubMed: 21387284]
4. Moraes MC, Neto JB, Menck CF. DNA repair mechanisms protect our genome from carcinogenesis. Front Biosci. 2012; 17:1362–1388. [PubMed: 22201809]
5. Cadet J, Douki T, Ravanat JL. One-electron oxidation of DNA and inflammation processes. Nat Chem Biol. 2006; 2:348–349. [PubMed: 16783334]
6. Steenken S, Jovanovic SV. How easily oxidizable is DNA? One-electron reduction potentials of adenosine and guanosine radicals in aqueous solution. J Am Chem Soc. 1997; 119:617–618.
7. Cadet J, Douki T, Ravanat JL. Oxidatively generated damage to the guanine moiety of DNA: Mechanistic aspects and formation in cells. Acc Chem Res. 2008; 41:1075–1083. [PubMed: 18666785]
8. Collins AR, Cadet J, Moller L, Poulsen HE, Vina J. Are we sure we know how to measure 8-oxo-7,8-dihydroguanine in DNA from human cells? Arch Biochem Biophys. 2004; 423:57–65. [PubMed: 14989265]
9. Steenken S, Jovanovic SV, Bietti M, Bernhard K. The trap depth (in DNA) of 8-oxo-7,8-dihydro-2′deoxyguanosine as derived from electron-transfer equilibria in aqueous solution. J Am Chem Soc. 2000; 122:2373–2374.
10. Fleming AM, Muller JG, Dlouhy AC, Burrows CJ. Structural context effects in the oxidation of 8-oxo-7,8-dihydro-2′-deoxyguanosine to hydantoin products: Electrostatics, base stacking, and base pairing. J Am Chem Soc. 2012; 134:15091–15102. [PubMed: 22880947]
11. Luo W, Muller JG, Rachlin EM, Burrows CJ. Characterization of spiroiminodihydantoin as a product of one-electron oxidation of 8-oxo-7,8-dihydroguanosine. Org Lett. 2000; 2:613–616. [PubMed: 10814391]

12. Luo W, Muller JG, Rachlin EM, Burrows CJ. Characterization of hydantoin products from one-electron oxidation of 8-oxo-7,8-dihydroguanosine in a nucleoside model. Chem Res Toxicol. 2001; 14:927–938. [PubMed: 11453741]

13. Niles JC, Wishnok JS, Tannenbaum SR. Spiroiminodihydantoin is the major product of the 8-oxo-7,8-dihydroguanosine reaction with peroxynitrite in the presence of thiols and guanosine photooxidation by methylene blue. Org Lett. 2001; 3:963–966. [PubMed: 11277770]

14. Henderson PT, Delaney JC, Muller JG, Neeley WL, Tannenbaum SR, Burrows CJ, Essigmann JM. The hydantoin lesions formed from oxidation of 7,8-dihydro-8-oxoguanine are potent sources of replication errors in vivo. Biochemistry. 2003; 42:9257–9262. [PubMed: 12899611]

15. Leipold MD, Muller JG, Burrows CJ, David SS. Removal of hydantoin products of 8-oxoguanine oxidation by the Escherichia coli DNA repair enzyme, FPG. Biochemistry. 2000; 39:14984–14992. [PubMed: 11101315]

16. Hazra TK, Muller JG, Manuel RC, Burrows CJ, Lloyd RS, Mitra S. Repair of hydantoins, one electron oxidation product of 8-oxoguanine, by DNA glycosylases of Escherichia coli. Nucleic Acids Res. 2001; 29:1967–1974. [PubMed: 11328881]

17. Hailer MK, Slade PG, Martin BD, Rosenquist TA, Sugden KD. Recognition of the oxidized lesions spiroiminodihydantoin and guanidinohydantoin in DNA by the mammalian base excision repair glycosylases NEIL1 and NEIL2. DNA Repair (Amst). 2005; 4:41–50. [PubMed: 15533836]

18. Krishnamurthy N, Zhao X, Burrows CJ, David SS. Superior removal of hydantoin lesions relative to other oxidized bases by the human DNA glycosylase hNEIL1. Biochemistry. 2008; 47:7137–7146. [PubMed: 18543945]

19. Zhao X, Krishnamurthy N, Burrows CJ, David SS. Mutation versus repair: NEIL1 removal of hydantoin lesions in single-stranded, bulge, bubble, and duplex DNA contexts. Biochemistry. 2010; 49:1658–1666. [PubMed: 20099873]

20. Hailer MK, Slade PG, Martin BD, Sugden KD. Nei deficient Escherichia coli are sensitive to chromate and accumulate the oxidized guanine lesion spiroiminodihydantoin. Chem Res Toxicol. 2005; 18:1378–1383. [PubMed: 16167829]

21. Mangerich A, Knutson CG, Parry NM, Muthupalani S, Ye W, Prestwich E, Cui L, McFaline JL, Mobley M, Ge Z, Taghizadeh K, Wishnok JS, Wogan GN, Fox JG, Tannenbaum SR, Dedon PC. Infection-induced colitis in mice causes dynamic and tissue-specific changes in stress response and DNA damage leading to colon cancer. Proc Natl Acad Sci U S A. 2012; 109:E1820–E1829. [PubMed: 22689960]

22. Ravanat JL, Cadet J. Reaction of singlet oxygen with 2′-deoxyguanosine and DNA. Isolation and characterization of the main oxidation products. Chem Res Toxicol. 1995; 8:379–388. [PubMed: 7578924]

23. Durandin A, Jia L, Crean C, Kolbanovskiy A, Ding S, Shafirovich V, Broyde S, Geacintov NE. Assignment of absolute configurations of the enantiomeric spiroiminodihydantoin nucleobases by experimental and computational optical rotatory dispersion methods. Chem Res Toxicol. 2006; 19:908–913. [PubMed: 16841958]

24. Ding S, Jia L, Durandin A, Crean C, Kolbanovskiy A, Shafirovich V, Broyde S, Geacintov NE. Absolute configurations of spiroiminodihydantoin and allantoin stereoisomers: Comparison of computed and measured electronic circular dichroism spectra. Chem Res Toxicol. 2009; 22:1189–1193. [PubMed: 19485408]

25. Ding S, Kolbanovskiy A, Durandin A, Crean C, Shafirovich V, Broyde S, Geacintov NE. Absolute configurations of DNA lesions determined by comparisons of experimental ECD and ORD spectra with DFT calculations. Chirality. 2009; 21(Suppl 1):E231–241. [PubMed: 19937959]

26. Jia L, Shafirovich V, Shapiro R, Geacintov NE, Broyde S. Spiroiminodihydantoin lesions derived from guanine oxidation: Structures, energetics, and functional implications. Biochemistry. 2005; 44:6043–6051. [PubMed: 15835893]

27. Jia L, Shafirovich V, Shapiro R, Geacintov NE, Broyde S. Structural and thermodynamic features of spiroiminodihydantoin damaged DNA duplexes. Biochemistry. 2005; 44:13342–13353. [PubMed: 16201759]

28. Jia L, Shafirovich V, Geacintov NE, Broyde S. Lesion specificity in the base excision repair enzyme hNeil1: Modeling and dynamics studies. Biochemistry. 2007; 46:5305–5314. [PubMed: 17432829]
29. Kornyushyna O, Berges AM, Muller JG, Burrows CJ. In vitro nucleotide misinsertion opposite the oxidized guanosine lesions spiroiminodihydantoin and guanidinohydantoin and DNA synthesis past the lesions using Escherichia coli DNA polymerase I (Klenow fragment). Biochemistry. 2002; 41:15304–15314. [PubMed: 12484769]
30. Kornyushyna O, Burrows CJ. Effect of the oxidized guanosine lesions spiroiminodihydantoin and guanidinohydantoin on proofreading by Escherichia coli DNA polymerase I (Klenow fragment) in different sequence contexts. Biochemistry. 2003; 42:13008–13018. [PubMed: 14596616]
31. Chinyengetere F, Jamieson ER. Impact of the oxidized guanine lesion spiroiminodihydantoin on the conformation and thermodynamic stability of a 15-mer DNA duplex. Biochemistry. 2008; 47:2584–2591. [PubMed: 18281959]
32. Joffe A, Geacintov NE, Shafirovich V. DNA lesions derived from the site-selective oxidation of guanine by carbonate radical anions. Chem Res Toxicol. 2003; 16:1528–1538. [PubMed: 14680366]
33. Crean C, Lee YA, Yun BH, Geacintov NE, Shafirovich V. Oxidation of guanine by carbonate radicals derived from photolysis of carbonatotetramminecobalt(III) complexes and the pH dependence of intrastrand DNA cross-links mediated by guanine radical reactions. Chem Bio Chem. 2008; 9:1985–1991.
34. Gremaud JN, Martin BD, Sugden KD. Influence of substrate complexity on the diastereoselective formation of spiroiminodihydantoin and guanidinohydantoin from chromate oxidation. Chem Res Toxicol. 2010; 23:379–385. [PubMed: 20014751]
35. Karwowski B, Dupeyrat F, Bardet M, Ravanat JL, Krajewski P, Cadet J. Nuclear magnetic resonance studies of the 4R and 4S diastereomers of spiroiminodihydantoin 2′-deoxyribonucleosides: absolute configuration and conformational features. Chem Res Toxicol. 2006; 19:1357–1365. [PubMed: 17040105]
36. Marky LA, Breslauer KJ. Calculating thermodynamic data for transitions of any molecularity from equilibrium melting curves. Biopolymers. 1987; 26:1601–1620. [PubMed: 3663875]
37. Kaushik M, Suehl N, Marky LA. Calorimetric unfolding of the bimolecular and i-motif complexes of the human telomere complementary strand, d(C3TA2)4. Biophys Chem. 2007; 126:154–164. [PubMed: 16822606]
38. Ganguly M, Wang F, Kaushik M, Stone MP, Marky LA, Gold B. A study of 7-deaza-2′-deoxyguanosine 2′-deoxycytidine base pairing in DNA. Nucleic Acids Res. 2007; 35:6181–6195. [PubMed: 17855404]
39. Courtenay ES, Capp MW, Anderson CF, Record MT Jr. Vapor pressure osmometry studies of osmolyte-protein interactions: implications for the action of osmoprotectants in vivo and for the interpretation of “osmotic stress” experiments in vitro. Biochemistry. 2000; 39:4455–4471. [PubMed: 10757995]
40. Ganguly M, Wang RW, Marky LA, Gold B. Thermodynamic characterization of DNA with 3-deazaadenine and 3-methyl-3-deazaadenine substitutions: the effect of placing a hydrophobic group in the minor groove of DNA. J Phys Chem B. 2010; 114:7656–7661. [PubMed: 20469878]
41. Shikiya R, Li JS, Gold B, Marky LA. Incorporation of cationic chains in the Dickerson-Drew dodecamer: Correlation of energetics, structure, and ion and water binding. Biochemistry. 2005; 44:12582–12588. [PubMed: 16156670]
42. Patel DJ, Pardi A, Itakura K. DNA conformation, dynamics, and interactions in solution. Science. 1982; 216:581–590. [PubMed: 6280281]
43. Patel DJ, Shapiro L, Hare D. DNA and RNA: NMR studies of conformations and dynamics in solution. Q Rev Biophys. 1987; 20:35–112. [PubMed: 2448843]
44. Van de Ven FJ, Hilbers CW. Nucleic acids and nuclear magnetic resonance. Eur J Biochem. 1988; 178:1–38. [PubMed: 3060357]
45. de los Santos C, Cosman M, Hingerty BE, Ibanez V, Margulis LA, Geacintov NE, Broyde S, Patel DJ. Influence of benzo[a]pyrene diol epoxide chirality on solution conformations of DNA covalent

adducts: the (−)-trans-anti-[BP]G.C adduct structure and comparison with the (+)-trans-anti-[BP]G.C enantiomer. Biochemistry. 1992; 31:5245–5252. [PubMed: 1606148]

46. Rentzeperis D, Kharakoz DP, Marky LA. Coupling of sequential transitions in a DNA double hairpin: energetics, ion binding, and hydration. Biochemistry. 1991; 30:6276–6283. [PubMed: 2059634]
47. Singh SK, Szulik MW, Ganguly M, Khutsishvili I, Stone MP, Marky LA, Gold B. Characterization of DNA with an 8-oxoguanine modification. Nucleic Acids Res. 2011; 39:6789–6801. [PubMed: 21572101]
48. Kankia BI, Soto AM, Burns N, Shikiya R, Tung CS, Marky LA. DNA oligonucleotide duplexes containing intramolecular platinated cross-links: energetics, hydration, sequence, and ionic effects. Biopolymers. 2002; 65:218–227. [PubMed: 12228927]
49. Marky LA, Rentzeperis D, Luneva NP, Cosman M, Geacintov NE, Kupke DW. Differential hydration thermodynamics of stereoisomeric DNA-benzo[a]pyrene adducts derived from diol epoxide enantiomers with different tumorigenic potentials. J Am Chem Soc. 1996; 118:3804–3810.
50. Spink CH, Chaires JB. Effects of hydration, ion release, and excluded volume on the melting of triplex and duplex DNA. Biochemistry. 1999; 38:496–508. [PubMed: 9890933]
51. Krishnamurthy N, Zhao X, Burrows CJ, David SS. Superior removal of hydantoin lesions relative to other oxidized bases by the human DNA glycosylase hNEIL1. Biochemistry. 2008; 47:7137–7146. [PubMed: 18543945]

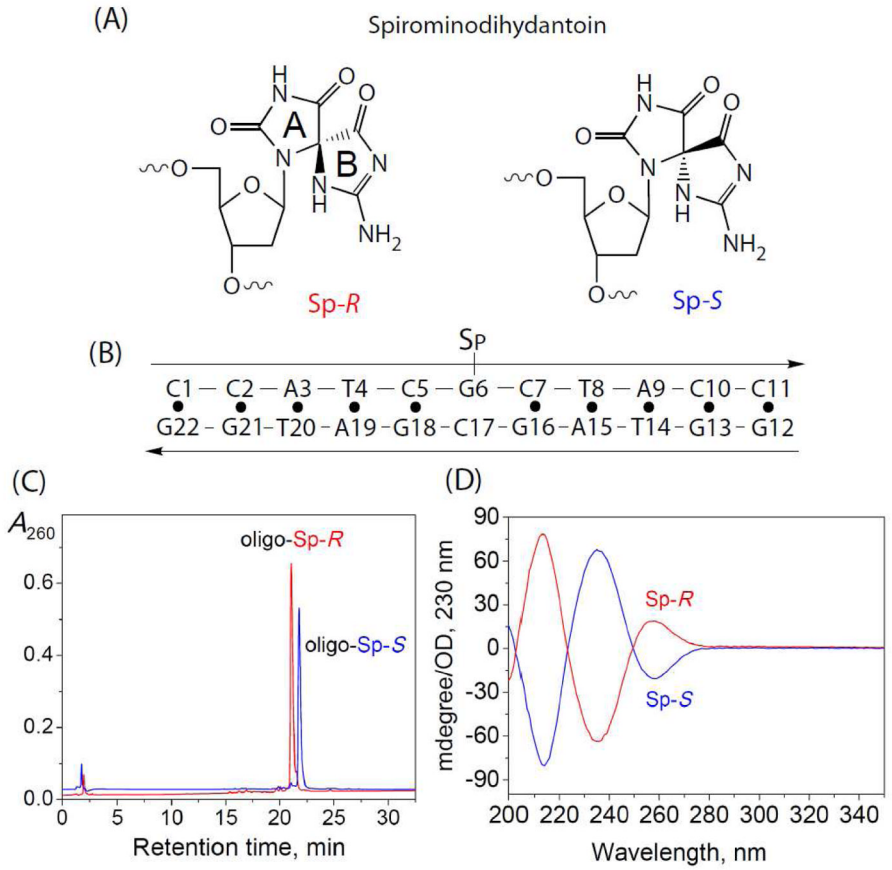

Figure 1.

(A) Structures of the Sp-*R* and Sp-*S* spiroiminodihydantoin diastereomers. (B) Base sequence of 11-mer duplexes. (C) Anion-exchange HPLC elution profile of 5′-CCATC[Sp-*R*]GCTACC and 5′-CCATC[Sp-*S*]GCTACC adducts. Conditions (analytical DNAPac PA-100 column, detection at 260 nm): 10 – 90% linear gradient of solvent B (10% acetonitrile and 90% 1.5 M ammonium acetate) in solvent A (10% acetonitrile and 90% water) for 30 min at a flow rate of 1 mL/min. (D) CD spectra of Sp-*R* and Sp-*S* nucleobases in water.

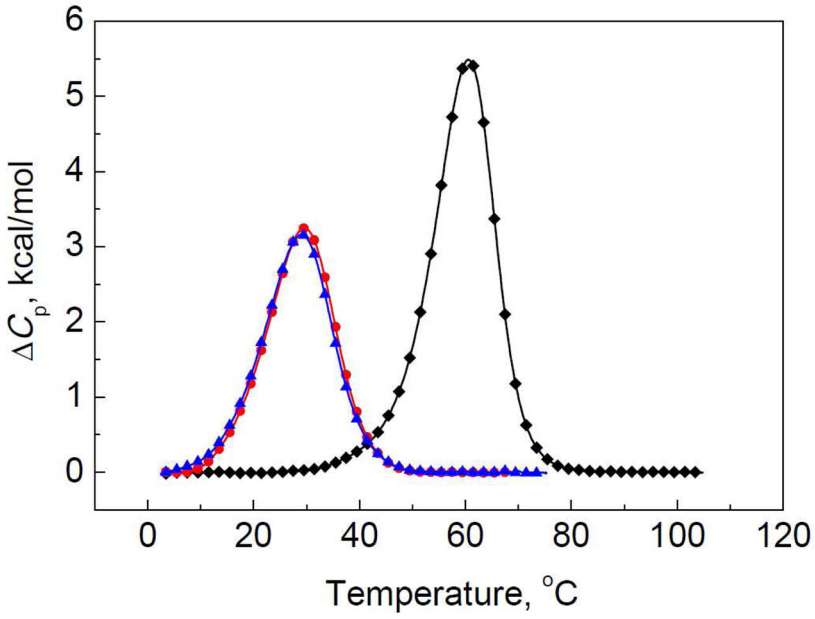

Figure 2.
Differential scanning calorimetry curves for each duplex in 20 mM sodium phosphate buffer containing 0.1M NaCl at pH 7, unmodified duplex (black), Sp-*R* (red), Sp-*S* (blue).

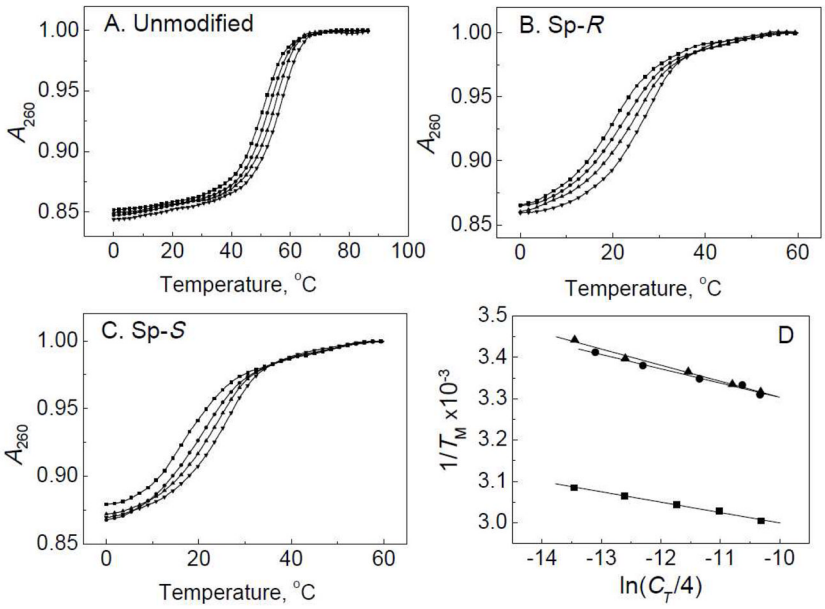

Figure 3.

Normalized UV melting curves of 11-mer duplexes with Sp-*R* or Sp-*S* lesions at different DNA concentrations in 20 mM sodium phosphate buffer solutions, 0.1 M NaCl, pH 7. (A) Unmodified DNA, concentrations: 5.7 μM (squares), 13.4 μM (circles), 32.3 μM (upward-pointing triangles), and 65.5 μM (downward-pointing triangles). (B) Sp-*R* duplex. DNA concentrations: 8.1 μM (squares), 18.2 μM (circles), 47.1 μM (upward-pointing triangles), and 96.7 μM (downward-pointing triangles). (C) Sp-*S* duplex. DNA concentrations: 5.8 μM (squares), 13.5 μM (circles), 38.9 μM (up triangles), and 81.8 μM (downward-pointing triangles). (D) Dependence of T_M on total DNA strand concentration, unmodified duplex (squares); Sp-*R* (circles), Sp-*S* (triangles).

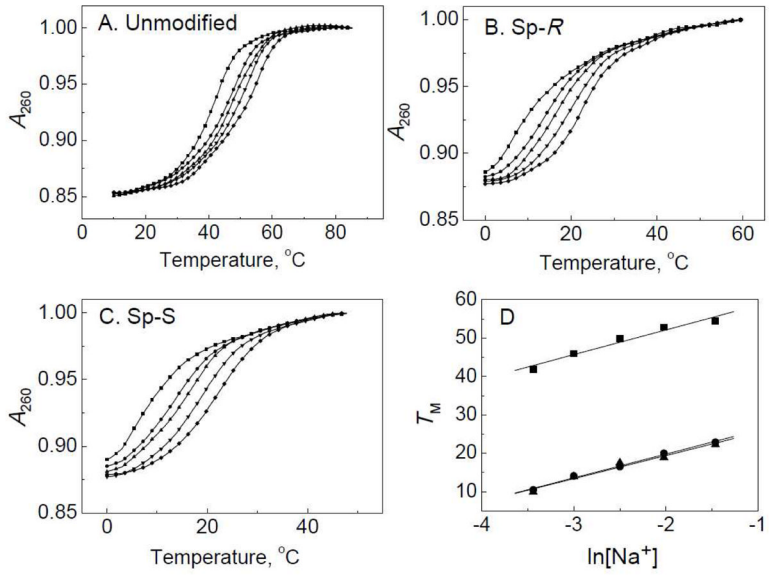

Figure 4.

Normalized UV melting curves of 11-mer duplexes with Sp-*R* or Sp-S lesions at different NaCl concentrations in 20 mM sodium phosphate buffer solutions, pH 7. (A) Unmodified duplex (5.7 μM in total strands), NaCl concentrations: 32 mM (squares), 50 mM (circles), 82 mM (upward-pointing triangles), and 135 mM (downward-pointing triangles), and 232 mM (diamonds). (B) Sp-*R* duplex (6.1 μM in total strands), NaCl concentrations: 32 mM (squares), 50 mM (circles), 82 mM (upward-pointing triangles), and 135 mM (downward-pointing triangles), 232 mM (diamonds). (C) Sp-*S* duplex (5.8 μM in total strands), NaCl: 32 mM (squares), 50 mM (circles), 82 mM (up triangles), and 135 mM (down triangles), and 232 mM (diamonds). (D) Dependence of T_M on NaCl concentration: unmodified duplex (squares), Sp-*R* (circles), Sp-*S* (triangles).

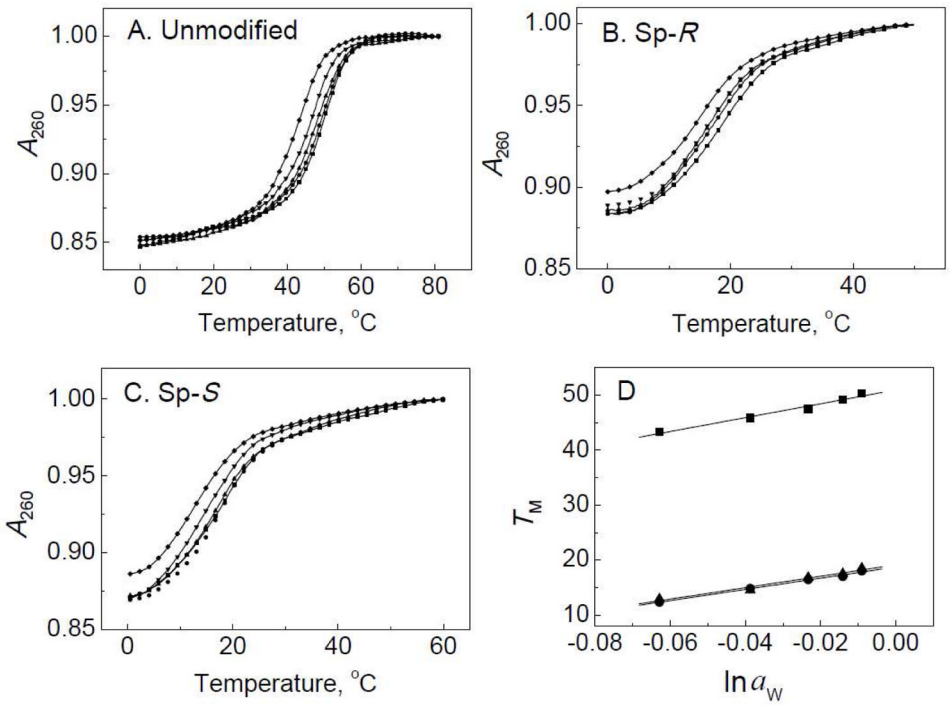

Figure 5.

Normalized UV melting curves of 11-mer duplexes with Sp-*R* or Sp-S lesions measured at the same DNA strand concentrations as in Figure 4 and with different ethylene glycol concentrations in 20 mM sodium phosphate buffer solutions, pH 7. (A) Unmodified duplex, ethylene glycol concentrations: 0.5 M (squares), 0.85 M (circles), 1.4 M (upward-pointing triangles), and 2.4 M (downward-pointing triangles), 4 M (diamonds). (B) Sp-*S* duplex, ethylene glycol concentrations: 0.5 M (squares), 0.85 M (circles), 1.4 M (upward-pointing triangles), and 2.4 M (downward-pointing triangles), 4 M (diamonds). (C) Sp-*R* duplex, ethylene glycol concentrations: 0.5 M (squares), 0.85 M (circles), 1.4 M (upward-pointing triangles), and 2.4 M (downward-pointing triangles), 4 M (diamonds). (D) Dependence of T_M on water activity: unmodified duplex (squares), Sp-*R* duplex (circles), Sp-*S* duplex (triangles).

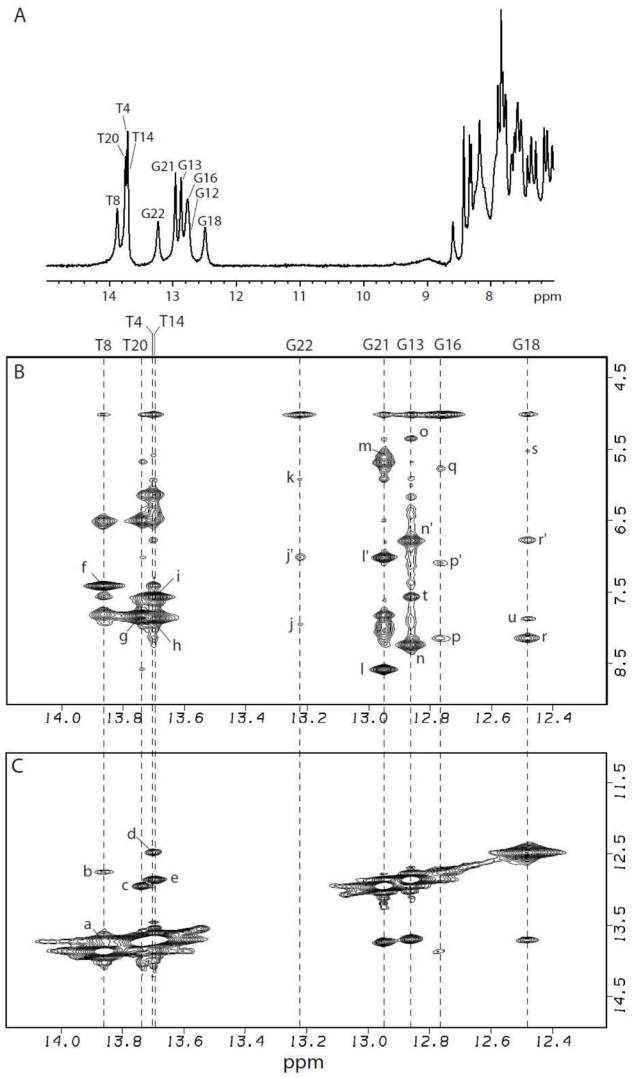

Figure 6.

Expanded 1D NMR spectrum and 2D NOESY spectra in the imino proton to amino and base proton region of the Sp-*R* duplex in 100 mM NaCl, 10 mM sodium phosphate containing 10% D_2O aqueous solution, pH 6.8, 0 °C. (A) 1D NMR spectrum (7.0–15.0 ppm); the imino proton assignments are shown. (B) Expanded NOESY (200 ms mixing time) contour plots for the Sp-*R* – containing 11-mer duplex. NOEs between imino protons (12.2 to 14.0 ppm), amino and non-exchangeable base protons (4.5 to 9.0 ppm), with NOE cross-peaks *f* to *u* characteristic of Watson-Crick base pairs. Cross-peaks *f* to *u* are assigned as follows: *f*, T8(NH3)-A15(H2); *g*, T20(NH3)-A3(H2); *h*, T4(NH3)-A19(H2); *i*, T14(NH3)-A9(H2); *j,j′*, G22(NH1)-C1(NH_2); *k*, G22(NH1)-C1(H5); *l,l′*, G21(NH1)-C2(NH_2); *m*, G21(NH1)-C2(H5); *n,n′*, G13(NH1)-C10(NH_2); *o*, G13(NH1)-C10(H5); *p,p′*, G16(NH1)-C7(NH_2); *q*, G16(NH1)-C7(H5); *r,r′*, G18(NH1)-C5(NH_2); *s*, G18(NH1)-C5(H5); *t*, G13(NH1)-A9(H2); *u*, G18(NH1)-A19(H2). (C) Expanded NOESY (200 ms mixing time) contour plot of the imino proton region (12 to 14 ppm) for the Sp-*R* – containing 11-mer duplex. Imino – imino proton NOEs, with the cross peaks labeled *a* to *e*, which are assigned as follows: *a*, T8(NH3)-T14(NH3); *b*, T8(NH3)-G16(NH1); *c*, T20(NH3)-G21(NH1); *d*, T4(NH3)-G18(NH1); *e*, T14(NH3)-G13(NH1).

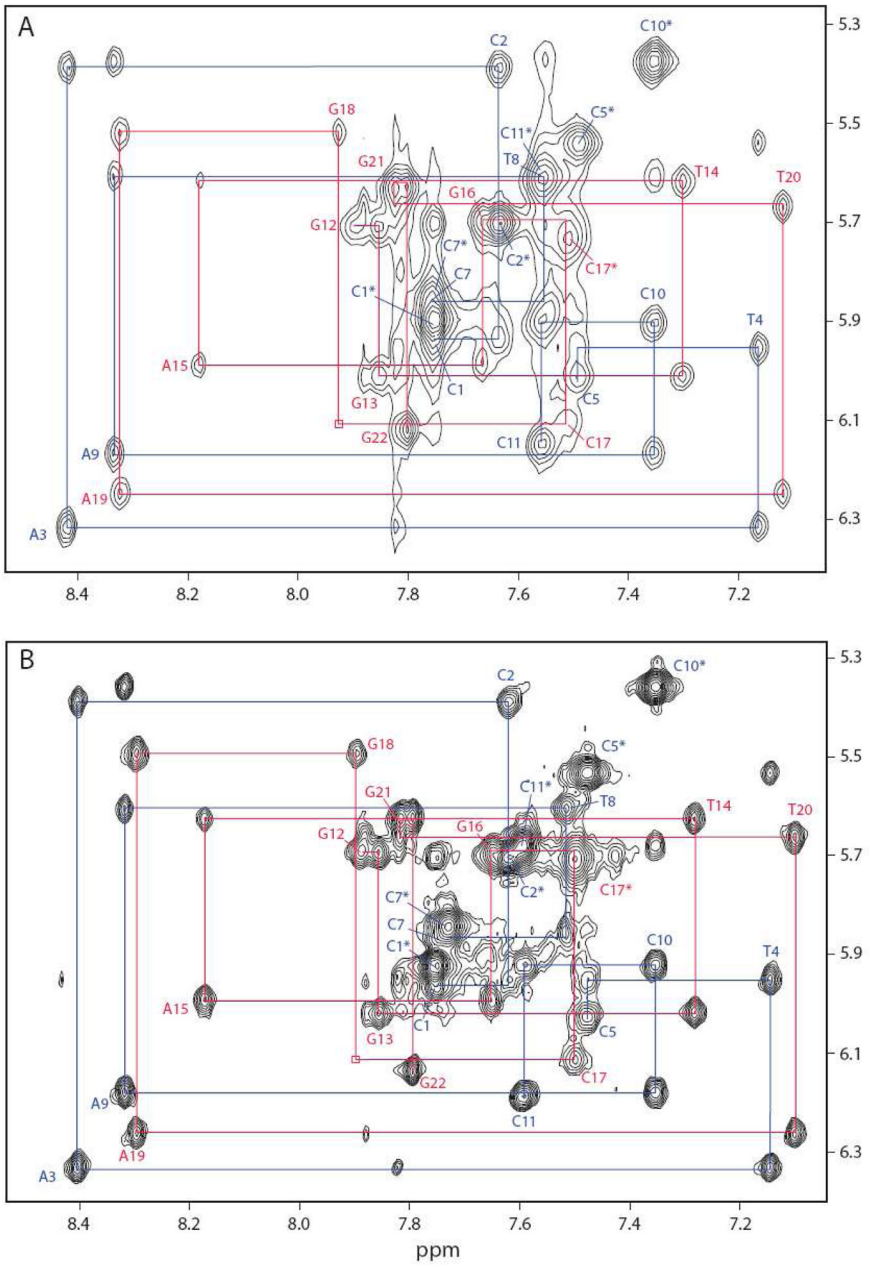

Figure 7.

Expanded NOESY (200 ms mixing time) contour plots for the Sp 11-mer duplexes in 100 mM NaCl, 10 mM sodium phosphate 100% D_2O buffer solution, pH 6.8, 10 °C. The NOE connectivities between base protons and their own and 5′-linked sugar H1′ protons are traced as blue lines for the Sp-modified strand, and as red lines in the case of the unmodified strand. The NOE cross-peaks between cytosine H6 and H5 protons are indicated by asterisks. (A) The Sp-*R* 11-mer duplex. The connectivities can be traced via identifiable NOEs from C1 – C5 and from C7 – C11 (blue lines), and from G12 – G22 (red lines). (B) The Sp-*S* 11-mer duplex. The connectivities can be traced via identifiable NOEs from C1 – C5 and from C7 – C11 (blue lines), and from G12 – G22 (red lines).

Table 1

Thermodynamic Profiles for the Unfolding of Oligonucleotide Duplexes.

Duplex	T_M (°C)	ΔH_{cal} (kcal/mol)	ΔH_{vH}^{cal} (kcal/mol)	ΔH_{vH}^{UV} (kcal/mol)	$T\Delta S_{cal}$ (kcal/mol)	$\Delta G_{(20)}^{cal}$ (kcal/mol)
Unmodified	59.8(±0.5)	82.9(±5)	78(±6)	79.5(±6)	73.0(±4)	9.9(±0.7)
Sp-*R*	29.2(±0.5)	54.0(±3)	59(±3)	53.1(±3)	52.4(±3)	1.6(±0.1)
Sp-*S*	28.6(±0.5)	53.4(±3)	58(±3)	51.2(±3)	51.9(±3)	1.5(±0.1)

Values were determined in 20 mM sodium phosphate buffer, 0.1M NaCl at pH7, the T_M values correspond to a duplex concentration of 130 μM (in total strands).

Table 2

Parameters Used to Calculate Differential of Counterion and Water Binding

Duplex	$RT_M^2/\Delta H$ **(K)**	$\partial T_M/\partial \ln[Na^+]$ **(K)**	Δn_{Na^+} **(mol$_{Na+}$/mol$_{dup}$)**	$\partial T_M/\partial \ln a_w$ **(K)**	Δn_w **(mol$_{Na+}$/mol$_{dup}$)**
unmodified	2.65	6.4	2.65	126.3	47.6
Sp-*R*	3.36	6.2	2.04	102.0	30.4
Sp-*S*	3.40	6.0	1.95	103.8	30.7

Table 3

Differential Thermodynamic Profiles for the Formation of Oligonucleotide Duplexes (using the unmodified duplex as a control, i.e. unmodified → modified.duplex)

Duplex	$\Delta\Delta G$ (kcal/mol)	$\Delta\Delta H$ (kcal/mol)	$\Delta(T\Delta S)$ (kcal/mol)	$\Delta\Delta n_{Na^+}$ (mol_{Na+}/mol_{dup})	$\Delta\Delta n_w$ (mol_{Na+}/mol_{dup})
Sp-*R*	8.3	28.9	20.6	0.6	17.2
Sp-*S*	8.4	29.5	21.1	0.7	16.9